Nano Research 2015, 8(5): 1443–1453
DOI 10.1007/s12274-014-0629-2
Research Article
ISSN 1998-0124
CN 11-5974/O4

Excellent photothermal conversion of core/shell CdSe/Bi_2Se_3 quantum dots

Guo Zhi Jia[1,2], Wen Kai Lou[1], Fang Cheng[3], Xiong Long Wang[4], Jiang Hong Yao[4], Ning Dai[5], Hai Qing Lin[6], and Kai Chang[1] (✉)

[1] *Institute of Semiconductors, Chinese Academy of Sciences, P.O. Box 912, Beijing 100083, China*
[2] *Tianjin Chengjian University, Tianjin 300384, China*
[3] *Department of Physics and Electronic Science, Changsha University of Science and Technology, Changsha 410004, China*
[4] *Key Laboratory of Weak-Light Nonlinear Photonics, Ministry of Education, School of Physics and TEDA Applied Physics School, Nankai University, Tianjin 300457, China*
[5] *The National Laboratory for Infrared Physics, the Shanghai Institute of Technical Physics of the Chinese Academy of Sciences, Shanghai 200083, China*
[6] *Beijing Computational Science Research Center, Beijing, 100084, China*

Received: 9 July 2014
Revised: 27 October 2014
Accepted: 30 October 2014

KEYWORDS
cation exchange,
quantum dots,
photothermal,
type-II heterostructure,
CdSe/Bi_2Se_3

ABSTRACT

Water-dispersed CdSe/Bi_2Se_3 core/shell QDs with a photothermal conversion coefficient of 27.09% have been synthesized by a cation exchange reaction. The microstructure and crystal structure of the QDs, which were confirmed by TEM and XRD, showed that partial cation exchange occurred inside the CdSe QDs. Two main mechanisms are responsible for the excellent photothermal conversion: inhibition of radiative recombination of carriers due to the formation of type-II semiconductor heterostructures, and the large surface-to-volume ratio of the QDs. Photothermal conversion experiments indicated that the CdSe/Bi_2Se_3 QDs showed high photothermal conversion efficiency and excellent NIR photostability.

1 Introduction

The photothermal effect has attracted extensive interest in recent years due to its potential application in nanoscale heat sources [1], biological imaging [2, 3], spectroscopy [4], drug delivery [5], nanocatalysis [6], and photothermal cancer therapy [7–21]. Most recent studies have focused on photothermal effects in noble metal nanoparticles caused by surface plasmon polaritons (SPP). The strong interaction between light and noble metal nanoparticles can change transient electron processes in atoms and molecules in biological

Address correspondence to kchang@semi.ac.cn

systems through SPPs [7, 10, 13, 15, 18, 19, 21]. Optically excited noble metal nanoparticles can be used as nanoscale heat sources through dissipation of absorbed light into thermal energy. Plasmon enhanced metal nanoparticles can therefore be used in photothermal cancer therapy.

Here, we suggest a new direction for photothermal effects in semiconductor nanostructures based on band engineering. We demonstrate that CdSe/Bi_2Se_3 core/shell quantum dots (QDs) can be developed for photothermal ablation (PTA) to replace the traditional therapeutic approaches to treat and control cancers, and can effectively avoid harming healthy cells and destroying the immune system [22]. This is mainly based on the fact that CdSe/Bi_2Se_3 QDs have a large absorption coefficient and high photothermal conversion efficiency in the near-infrared (NIR, λ = 700–1,100 nm) wavelengths. Near-infrared (NIR) irradiation undergoes relatively low scattering and absorption, and penetrates several centimeters into biological tissues [7, 18]. In addition, Bi and Se belong to the class of promising bio-friendly elements and Bi_2Se_3 has low cytotoxicity [23–25]. This suggests that Bi_2Se_3 is a promising photothermal agent and has potential applications in cancer therapy by photothermal techniques. Recently Bi_2X_3 (X = Se, Te, …), known as topological insulators, have attracted enormous attention in condensed matter physics because of their unique electronic properties. Topological insulators are a class of quantum materials possessing metallic surface states and insulating bulk crystals [26–31]. The enhanced thermoelectric performance of topological insulators has attracted extensive interest since the helical edge and surface states can provide ballistic channels for electrons [32]. The figure of merit (ZT) is expected to be larger than 1 in these materials.

Due to the unique advantages of PTA therapy, various NIR photothermal agents have been developed for cancer therapy, such as organic compounds [14], carbon-based materials [11, 20, 33], noble metal nanostructures [7, 34–36], and semiconductor compounds [12, 16, 18, 37]. Although noble metal nanostructures are the most widely studied agents and have large optical extinction coefficients and good photothermal conversion efficiency because of their tunable surface plasmon resonance (SPR) properties in the NIR wavelength, some substantial shortcomings impose limitations in their wide therapeutic applications: for example, their size is too large to increase bloodstream circulation times [38, 39], they lack good photothermal stability [17], and they require expensive raw materials. Previous studies have shown that few-layer Bi_2Se_3 can significantly enhance the contribution of exotic surface states due to its large surface-to-volume ratios [40]. Low-dimensional semiconductor nanostructures can effectively suppress bulk effects and lead to some novel physical properties. Layered or layered-like Bi_2Se_3 nanostructures have been fabricated by various methods for potential applications in spintronic devices. More recently, Bi_2Se_3 nanoplates as a new photothermal coupling agent for PTA of cancer cells have been utilized for enhanced X-ray computed tomography imaging of tumor tissue *in vivo* [22]. However, the large size of typical Bi_2Se_3 nanoplates, with an average diameter of about 90 nm, restricts their further bioapplications. Generally, a nanoparticle size between 10 and 50 nm is required for intravenous injection in order to increase bloodstream circulation times [17]. To the best of our knowledge, no synthesis method has been developed for Bi_2Se_3 nanomaterials with the optimum size and biocompatibility for application in biomedical fields.

In this communication, we report the first example of water-dispersed CdSe/Bi_2Se_3 core/shell QDs which can be rapidly synthesized by a cation exchange method assisted by ultrasonic irradiation, as shown in Fig. 1(a). As-prepared CdSe/Bi_2Se_3 QDs not only possess high photothermal conversion efficiency at a wavelength of 808 nm, but also excellent photostability and favorable biocompatibility due to the QDs having a thiol-stabilized surface. These features are attributed to the type-II QDs heterostructure and large surface-to-volume ratio of the QDs.

2 Experimental

2.1 Synthesis of CdSe QDs

Selenium powder, $CdCl_2{\cdot}2.5H_2O$, Na_2SO_3, $Bi(NO_3)_3{\cdot}5H_2O$, and thioglycolic acid (TGA), were AR. Ultrapure water and a microwave system (MAS-I) was used for the synthesis of CdSe QDs, and an ultrasound system (KQ2200DE) for the synthesis of Bi_2Se_3. CdSe QDs were synthesized according to the literature. Briefly, Se powder (0.0632 g), Na_2SO_3 (0.3025 g) and 40 mL of water were added into a 100 mL flask. The mixture

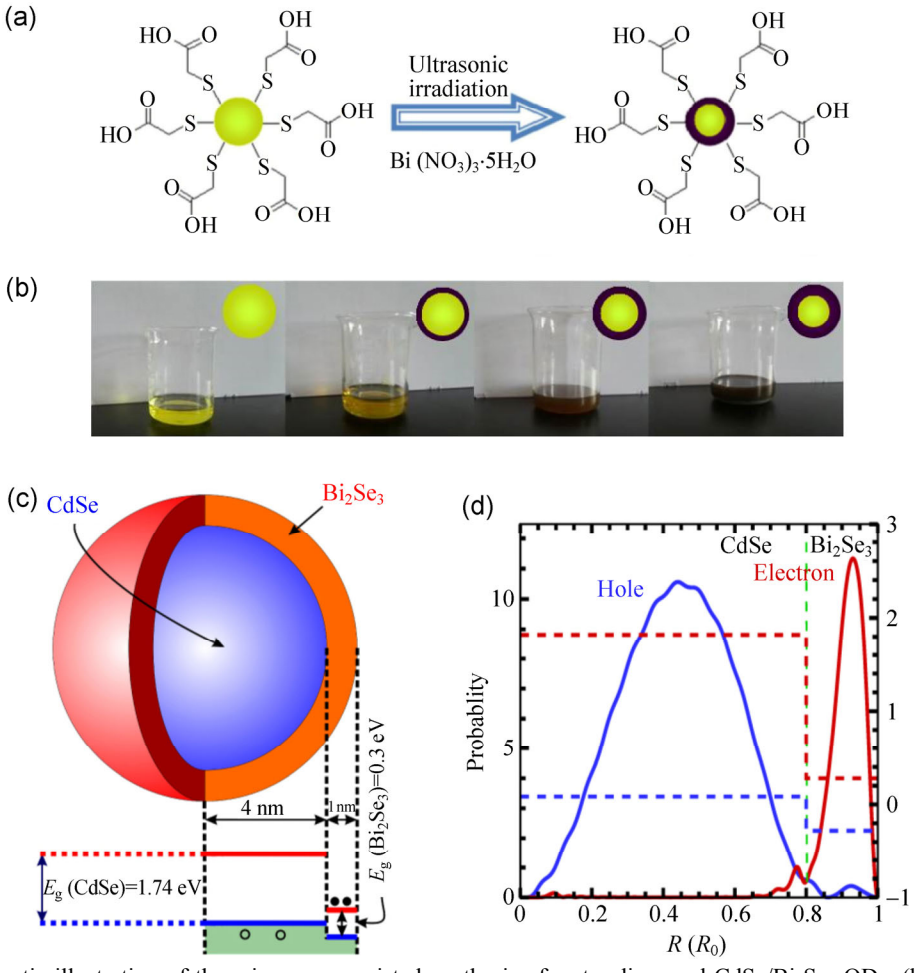

Figure 1 (a) Schematic illustration of the microwave-assisted synthesis of water-dispersed CdSe/Bi_2Se_3 QDs. (b) Photograph of the QD solutions. (c) Schematic band profile of the core/shell QDs. (d) The spatial distribution of electron and hole states in the core/shell QDs.

was stirred vigorously at 80 ℃ under a nitrogen atmosphere. After 3 h, a transparent Na_2SeSO_3 solution was obtained. $CdCl_2·2.5H_2O$ (0.2740 g) was completely dissolved in 100 mL of water, and then 5 drops of TGA was added dropwise to the $CdCl_2$ solution. The solution quickly became milk white when TGA was added. 10 mL of 1 M NaOH solution was employed to adjust the pH value of $CdCl_2$ solution to about 8. When the NaOH was added into $CdCl_2$ solution, the white precipitate disappeared and the solution became transparent again at pH 7. Nitrogen gas was used to deaerate oxygen for at least 30 min and the $CdCl_2$ precursor was obtained. Under N_2 protection, the Na_2SeSO_3 solution was injected into the $CdCl_2$ precursor and mixed well. The mixture was transferred into the microwave system. CdSe QDs solution was prepared after microwave irradiation (1,000 W) for 5 min at 100 ℃.

2.2 Cation exchange reaction

$Bi(NO_3)_3·5H_2O$ was added to the QDs solution and the mixture transferred into the ultrasound system. When the solid $Bi(NO_3)_3·5H_2O$ was added slowly, the mixture changed from white to dark brown. After ultrasonic irradiation for 5 min, the solid was dissolved and the color of QDs became dark red. No precipitate was observed in the solution. 30 mL of acetone was added to the solution and a precipitate appeared. After centrifuging and washing three times, the precipitate was collected and dried. A black powder was obtained.

2.3 Characterization

UV–vis absorption spectra were obtained using a Perkin Lambda UV–vis–NIR spectrophotometer. Transmission electron microscopy (TEM) and high-resolution TEM (HRTEM) images were recorded on a JEOL microscope

operated at 200 kV. All optical measurements were performed at room temperature under ambient conditions.

2.4 Photothermal conversion

For measuring the photothermal conversion performance of CdSe/Bi_2Se_3 core/shell QDs, an 808 nm NIR laser beam (from an adjustable power 808 nm semiconductor laser) was delivered through a quartz cuvette containing an aqueous dispersion (1.0 mL) of samples with the same QD concentrations. The output power was independently calibrated using an optical power meter and was found to be 1.6 W for a spot size of ~0.6 cm^2. A thermocouple with an accuracy of ±0.1 ℃ was inserted into the aqueous dispersion of the QDs perpendicular to the path of the laser. The temperature was recorded every 10 s.

3 Results and discussion

CdSe nanocrystals were chose as the QD core due to their mature preparation technology and the high degree of control over size and shape that can be achieved. Water-dispersed CdSe QDs were first synthesized via microwave irradiation. The size and shape of the CdSe QDs can be controlled by changing the experimental conditions. CdSe/Bi_2Se_3 core/shell QDs were subsequently formed by ultrasonic wave-assisted cation exchange reactions. The Bi^{3+} ions substitute Cd^{2+} ions to yield CdSe/Bi_2Se_3 QDs by a cation exchange reaction. Ion exchange reactions depend sensitively on the size and shape of the nanocrystals involved [41, 42]. Small QDs with a large surface-to-volume ratio favor the cation exchange reaction and lower the phase transition temperatures due to the lower activation energies for the diffusion of atoms and ions in the QDs [42]. Bi^{3+} ions are slightly larger than Cd^{2+} ions, which kinetically hinders the cation exchange reaction at ambient temperature. As shown in Fig. 1(b), the color of the solution gradually changed from yellow-green to black with increasing concentration of $Bi(NO_3)_3{\cdot}5H_2O$ under ultrasonic irradiation, indicating the cation exchange reaction was occurring, leading to the formation of the Bi_2Se_3 shell. For larger size CdSe QDs, we found the cation exchange to be virtually prohibited for similar irradiation power and time. This confirms that the reaction energy barrier is much lower for small sized crystals than for larger systems, even in the case of nanostructure QDs. In addition, although the anion sublattice determines the structural framework of the crystal, it is conceivable that the large size of the Bi^{3+} ions and the energy of ultrasonic irradiation can substantially influence the structure of the crystal during the cation exchange process under ultrasonic irradiation.

In previous studies, it was shown that the interface and surface states become more important as the size of the QDs decreases. Usually the dominant effect is the quantum confinement effect for small QDs, but the band alignment (or band offsets) is assumed to be the same as that in the bulk case in the most of theoretical models [43–45]. A schematic energy diagram of the CdSe/Bi_2Se_3 core/shell QDs under investigation is shown in Fig. 1(c). From the energy band alignments it can be clearly seen that CdSe/Bi_2Se_3 core/shell QDs show a typical type-II band alignment, which means that holes are localized in the core region, while electrons are confined in the shell region. In addition, the Bi_2Se_3 shell also possesses states localized near the surface, in contrast to conventional semiconductor QDs. The spatial distribution of electron and hole states in the core/shell QDs were calculated according to the multi-band low energy $k{\cdot}p$ model [26]. It can be clearly seen that the electrons and holes are localized in different regions, resulting in the formation of a type-II semiconductor heterostructure, as shown in Fig. 1(d). When the electron and hole pairs in the Bi_2Se_3 shell are excited by the 808 nm laser, the photo-excited holes will relax into the core region. The spatial separation between electron and hole states results in a very low recombination rate, i.e., a long lifetime of electron–hole pairs [46]. Notice that the bottom of the conduction band of Bi_2Se_3 is slightly higher than the top of the valence band of CdSe, and therefore almost all of the energy of the electron–hole pairs gained from the laser will be released into the crystal system, leading to an increase in the crystal temperature.

Since the Bi_2Se_3 shell layer is formed from a CdSe alloy with random substitution of Cd^{2+} ions at the

surface of the CdSe nanocrystal, the photo-excited electrons can be trapped and spatially separated by the electron and hole states in the core or shell regions, which leads to an increased electron–hole pair lifetime. Recent experiments show that Bi_2Se_3 ultrathin films can open up a considerable bandgap and thus allow greater access to the exotic surface states [47–49]. However, it is very difficult to directly probe topological surface states in the ultrathin Bi_2Se_3 shell layer of the core/shell QDs by angle resolved photoemission spectroscopy (ARPES) and transport measurements. Therefore, it is not possible to determine the role of the surface states in the process of photothermal conversion.

The samples were analyzed by transmission electron microscopy (TEM). A high-resolution TEM image of the CdSe QDs is shown in Fig. 2(a) The HRTEM image is taken along the [0001] crystallographic direction, and clearly reveals crystalline lattice fringes. The as-grown CdSe QDs have an average radius of about 5 nm. The growth kinetics could not be finely controlled under the low temperature reaction conditions, which results in a relatively broad size distribution of the QDs. This broad size distribution should not have a crucial influence on the photothermal effect in core/shell QDs, since the key factor is the spatial separation of photo-excited electrons and holes caused by the type-II band alignment. After the cation exchange reaction, the HRTEM image (Fig. 2(b)) clearly shows that the parent lattice is retained and no obvious interface between the core and shells is observed, which indicates that the cation exchange reaction does not disturb the crystalline shape of the parent QDs. Energy-dispersive spectra (EDS) of samples before and after cation exchange, as shown in Fig. 2(c), confirm the presence of Cd, Se, and Bi elements, indicating that Bi^{3+} ions have successfully exchanged with Cd^{2+} ions. The nanocrystals were further characterized by X-ray powder diffraction (XRD) (Fig. 2(d)). All of the diffraction peaks from the samples (a) to (g) can be readily indexed to the zinc blende structure. The three strong peaks at 2θ angles of 23.78, 39.38, and 46.48 correspond to the (111), (220), and (311) planes, respectively. We do not observe any characteristic diffraction peak corresponding to the Bi_2Se_3 by Gaussian fitting of the (111) diffraction peak, which confirms the formation of a Bi_2Se_3 shell surrounding the CdSe core.

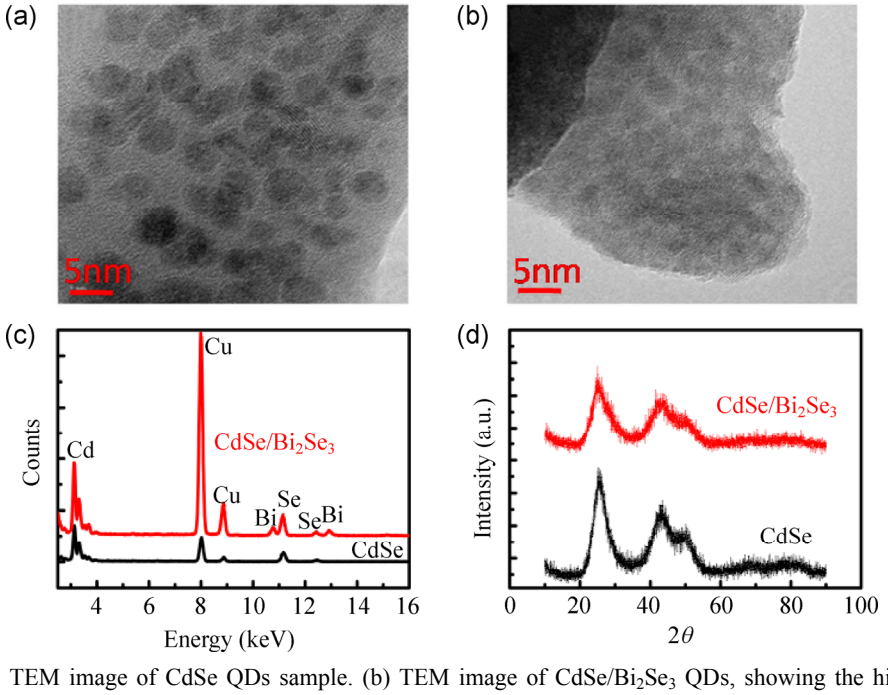

Figure 2 (a) Typical TEM image of CdSe QDs sample. (b) TEM image of $CdSe/Bi_2Se_3$ QDs, showing the high quality crystalline structure. (c) Energy-dispersive X-ray spectra of CdSe QDs and $CdSe/Bi_2Se_3$ core/shell QDs. (d) Powder X-ray diffraction patterns of the same samples.

Figure 3 shows the Fourier transform infrared (FTIR) spectra of the capping ligands on the surface of the QDs before and after exchange with Bi^{3+} ions. In both samples, a broad band at 3,450 cm^{-1} corresponds to the OH stretching vibration and the band around 1,710 cm^{-1} can be assigned to the C=O stretching vibration of TGA; in addition, the weak band at 1,030 cm^{-1} can be assigned to a C–S stretching vibration. This confirms that the products were capped with TGA through the reaction between Cd^{2+}/Bi^{3+} ions and thiol groups. As a result of the presence of the hydrophilic TGA ligands on the surface of the CdSe/Bi_2Se_3 QDs, aqueous dispersions of CdSe/Bi_2Se_3 QDs have high stability and even remain unchanged after being dispersed in water for one month, as shown in Fig. 1(b). It is reasonable to assume that the surface state of QDs can be effectively passivated by capping with TGA, indicating that no contribution to PT efficiency will arise from nonradiative recombination of the surface defects.

Figure 4 shows the UV–vis-NIR absorption spectra of aqueous dispersions of CdSe QDs before and after cation exchange reactions with different concentrations of $Bi(NO_3)_3{\cdot}5H_2O$ aqueous solution. Generally, the strong absorption of the nanocrystals results in an efficient photothermal conversion. In fact, as for other semiconductor nanocrystals, the photo-excited electron–hole pairs can relax through two dominant channels: nonradiative and radiative recombination. The nonradiative recombination process can mainly be ascribed to the defects produced during the fabrication process of the nanocrystals, which trap electrons or holes spatially and increase electron–hole lifetimes. The photothermal effect in type-I QDs mainly arises from the nonradiative phonons. The energy gained from light can be transferred to phonons leading to an increase in the crystal temperature. Usually, the lifetime of photo-excited electron–hole pairs in type-I QDs is quite short. This rapid recombination process strongly limits the photothermal effect. As the molar ratio of $Bi(NO_3)_3{\cdot}5H_2O$ was gradually increased, the absorbance intensity of the 808 nm band increased and became red-shifted. This indicates that the cation exchange process occurs from surface inwards to the core in CdSe QDs. The

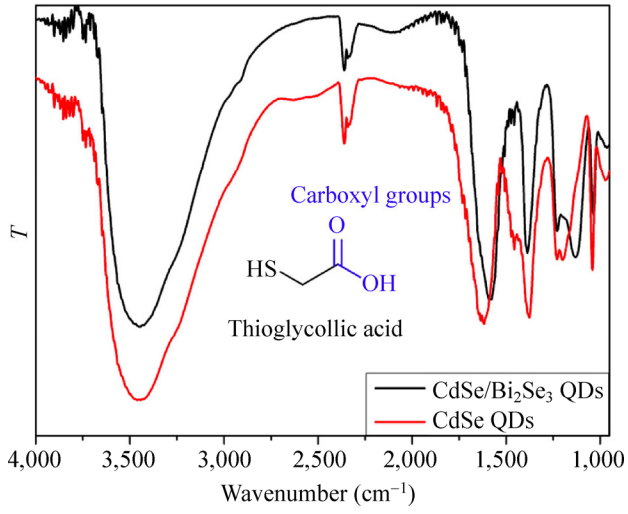

Figure 3 FTIR spectra of CdSe and CdSe/Bi_2Se_3 QDs.

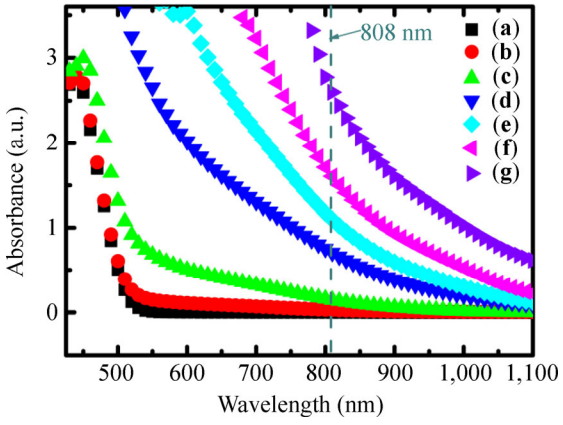

Figure 4 UV–vis–NIR absorption spectra of aqueous dispersions of CdSe QDs before and after cation exchange reaction with different molar amounts of $Bi(NO_3)_3{\cdot}5H_2O$: (**a**) 0 g; (**b**) 0.00485 g; (**c**) 0.0097 g; (**d**) 0.01455 g; (**e**) 0.02425 g; (**f**) 0.0291 g; and (**g**) 0.03395 g.

shift in absorbance edge can be attributed to the increase of the molar fraction of Bi^{3+} in the shell region of the QDs and the transformation to a heterostructure.

QDs having Bi_2Se_3 shells with different thickness were synthesized by reaction between CdSe QDs with various concentrations of $Bi(NO_3)_3{\cdot}5H_2O$ under irradiation with the same ultrasonic power and time. The photothermal effect of the samples was investigated by monitoring the temperature of 1 mL of aqueous solutions of materials with various Bi_2Se_3 shell thickness irradiated by a NIR laser (808 nm, 1.6 W), as shown in Fig. 5(a). The blank experiment demonstrates that the temperature of pure water is increased by less than 3 ℃. In the presence of QDs,

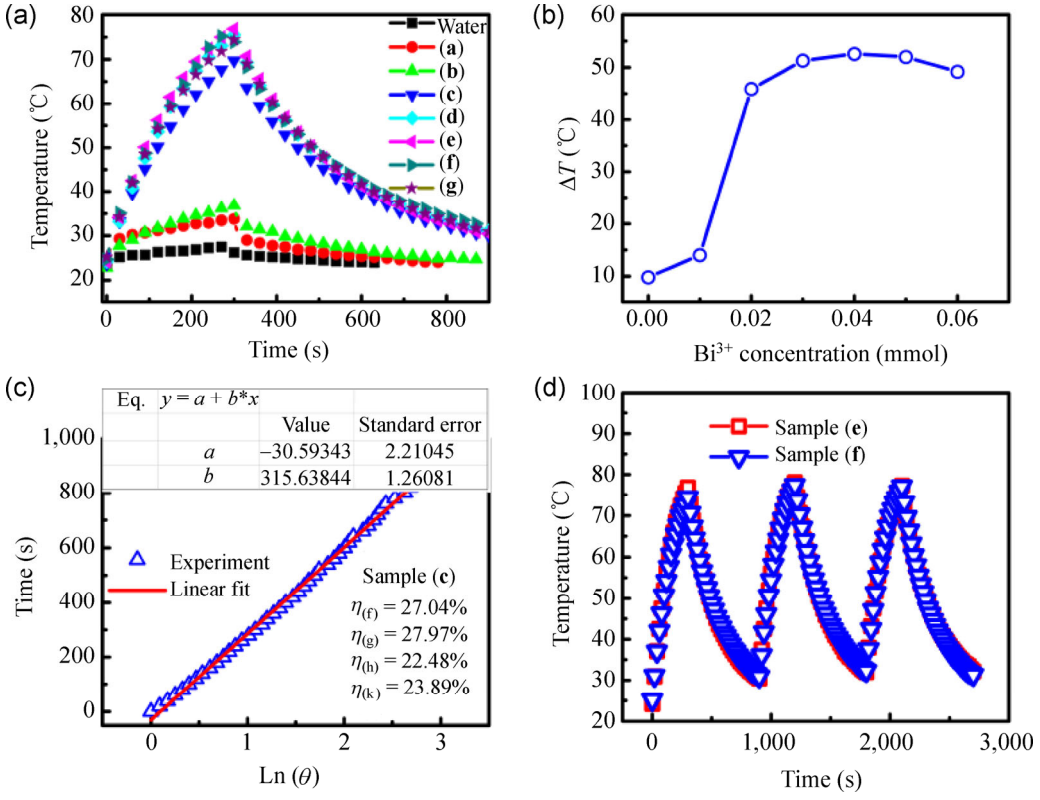

Figure 5 (a) Photothermal effect of the irradiation of aqueous dispersions of QDs with different thicknesses of Bi_2Se_3 shell using the NIR laser (808 nm, 1.6 W), with irradiation for 5 min, after which the laser was shut off. (**a**)–(**g**) correspondaqueous dispersions of CdSeQDs before and after cation exchange reaction with different molar weight of $Bi(NO_3)_3$: (**a**) 0 g, (**b**) 0.00485 g, (**c**) 0.0097 g, (**d**) 0.01455 g, (**e**) 0.02425 g, (**f**) 0.0291 and (**g**) 0.03395 g, respectively. (b) Plot of temperature change over a period of 5 min versus the different Bi^{3+} concentrations during the cation exchange reaction process. (c) The time constant for heat transfer from the system is determined to be τ_s = 315 s by plotting the linear time data from the cooling period (after 300 s) versus the negative natural logarithm of driving force temperature, which is obtained from the cooling stage of panel (a). (d) Temperature elevation of the typical CdSe/Bi_2Se_3 QDs for samples (e) and (f) over three laser ON/OFF cycles for 808 nm NIR laser irradiation.

the temperature of the aqueous dispersion increases rapidly, by as much as 50 ˚C in 5 min. As illustrated in Fig. 5(b), the temperature rise initially increases rapidly with increasing Bi_2Se_3 shell thickness, and then saturates with further increases of Bi_2Se_3 shell thickness. This saturation can be attributed to a fast heat loss at relatively high temperatures. Thus the observed temperature change is almost constant, even when the Bi_2Se_3 shell thickness is increased. The initial variation photothermal conversion efficiency indicates that the dominant photothermal conversion process is closely related to the process of cation exchange, i.e., the thickness of the Bi_2Se_3 shell. Bi^{3+} ions can appear at the surface of QDs by substituting for Cd^{2+} ions with a low concentration of Bi^{3+} ions in the reaction solution. A Bi_2Se_3 shell is gradually formed with increasing Bi^{3+} concentration. As the thickness of Bi_2Se_3 shell region increases, the QDs form type-II heterostructures. The lifetime of electron–hole pairs is enchanced significantly due to the reduction in bandgap from a direct bandgap to an indirect bandgap, and therefore most of the energy gained from the light will be converted into the phonon system, leading an increase in crystal temperature.

An ideal photothermal agent for biological applications should have excellent photothermal conversion efficiency and photostability. The photothermal conversion efficiency was calculated according to Roper's method and is independent of the shape of the nanocrystals in the aqueous dispersion [18, 37]. The temperature decrease of the solution was monitored in order to determine the heat transfer time constant from the dispersion system to surroundings. The heat conversion efficiencies are higher than 20% for

samples (d), (e), (g), and (f) (as defined in the legend to Fig. 4), which can be attributed to the strong NIR absorption and effective nonradiative electron relaxation dynamics (Fig. 5(c)). To investigate the NIR photostability of CdSe/Bi_2Se_3 QDs, three ON/OFF cycles of the NIR laser were employed. No significant decrease in the temperature elevation was observed in subsequent cycles indicating that the as-prepared CdSe/Bi_2Se_3 nanoparticles show excellent photostability (Fig. 5(d)). The excellent photothermal conversion ability and photostability of the CdSe/Bi_2Se_3 nanoparticles suggests that they should be able to act as photothermal agents to effectively destroy cancer cells.

In order to clearly understand the mechanism of PT conversion in type-II core/shell structure QDs, the carrier dynamics can be analyzed as follows. For type-I semiconductor QDs, the dominant PT conversion channels are defect-assisted recombination and phonon-mediated relaxation processes of electrons to bottom of the conduction band before radiative recombination. For the core/shell semiconductor QDs, the carrier lifetime and optical transition rate depend strongly on the energy band alignments of the semiconductor heterostructures. There are two important features characteristic of a type-II band alignment. First, one can see clearly that additional Bi_2Se_3 shell growth leads to a red-shift of the absorption band edge beyond the band edge of bulk CdSe (1.75 eV) (Fig. 4), which is important evidence for type-II band alignment with the increasing Bi_2Se_3 shell thickness [50]. In addition, it can be clearly seen that the photothermal conversion exhibits an abrupt increase as the Bi_2Se_3 thickness increases (Fig. 5(a)). These two features can be ascribed to the significant increase in carrier lifetimes due to the spatial separation of the carriers, i.e., a type-II band alignment [46, 51]. The excess energy of photo-excited electron–hole pairs is much larger than the narrow bandgap, and therefore the excess energy will heat the QD crystals through phonon emission. Almost all the energy of electron–hole pairs gained from the light will be converted into the phonon system, since the bottom of the conduction band of the Bi_2Se_3 shell is only slightly higher than the top of the valence band of the CdSe core. Usually, for photo-excited electron–hole pairs in narrow band gap semiconductors, the excess kinetic energy can create an effective temperature which is much higher than the lattice temperature. In type-II QDs, spatially separated carriers are localized in the two different regions (the core or shell regions) due to the type-II band alignment (Fig. 1(d)) [47, 52–54]. The Auger and radiative decay lifetimes can be very long for such spatially separated electron–hole pairs [55]. The spatial separation can effectively inhibit radiative recombination of the carriers and increase their lifetime, which results in a temperature equilibrium between carriers and the crystal, i.e., highly efficient photothermal conversion.

4 Conclusion

Water-dispersed CdSe/Bi_2Se_3 core/shell QDs with a photothermal conversion coefficient of 27.09% have been synthesized by a cation exchange reaction. The formation of CdSe/Bi_2Se_3 core/shell QDs was confirmed by TEM and XRD, showing that cation exchange occurred inside the CdSe QDs. The radiative recombination of carriers can be inhibited due to the formation of a type-II semiconductor heterostructure. The photothermal conversion experiment results indicate that the CdSe/Bi_2Se_3 nanoparticles show high photothermal conversion efficiency and excellent NIR photostability.

Acknowledgements

This work has been partly supported by the National Basic Research Program of China (973 Program) No. 2011CB922204-2, and the National Natural Science Foundation of China (Nos. 11434010, 11147024, 11247025, 11304306, 11374002, and 61290303).

Electronic Supplementary Material: Supplementary material (details of the macroscopic model for calculating photothermal efficiencies and heat transfer time constant) is available in the online version of this article at http://dx.doi.org/ 10.1007/s12274-014-0629-2.

References

[1] Zhang, W. C.; Li, Q.; Qiu, M. A plasmon ruler based on nanoscale photothermal effect. *Opt. Express* **2013**, *21*, 172–181.

[2] Ting, L.; Tian, J. G.; Chen, Z. L.; Liang, Y.; Liu, J.; Liu, S.; Li, J. H.; Zhan, J. H.; Yang, X. S. Anti-TROP$_2$ conjugated hollow gold nanospheres as a novel nanostructure for targeted photothermal destruction of cervical cancer cells. *Nanotechnology* **2014**, *25*, 345103.

[3] Yim, J. Y.; Kim, H.; Ryu, S.; Song, S. W.; Kim, H. O.; Hyun, K.-A.; Jung, H.-I.; Joo, C. Photothermal spectral-domain optical coherence reflectometry for direct measurement of hemoglobin concentration of erythrocytes. *Biosens. Bioelectron.* **2014**, *57*, 59–64.

[4] Strzalkowski, K.; Zakrzewski, J.; Maliński, M. Determination of the exciton binding energy using photothermal and photoluminescence spectroscopy. *Int. J. Thermophys.* **2013**, *34*, 691–700.

[5] Wang, Z. Z.; Chen, Z. W.; Liu, Z.; Shi, P.; Dong, K.; Ju, E. G.; Ren, J. S.; Qu, X. G. A multi-stimuli responsive gold nanocage-hyaluronic platform for targeted photothermal and chemotherapy. *Biomaterials* **2014**, *35*, 9678–9688.

[6] Byeon, J. H.; Kim, Y.-W. Au–TiO$_2$ nanoscale heterodimers synthesis from an ambient spark discharge for efficient photocatalytic and photothermal activity. *ACS Appl. Mater. Interfaces* **2014**, *6*, 763–767.

[7] Chen, J. Y.; Glaus, C.; Laforest, R.; Zhang, Q.; Yang, M. X.; Gidding, M.; Welch, M. J.; Xia, Y. N. Gold nanocages as photothermal transducers for cancer treatment. *Small* **2010**, *6*, 811–817.

[8] Chu, M. Q.; Pan, X. J.; Zhang, D.; Wu, Q.; Peng, J. L.; Hai, W. X. The therapeutic efficacy of CdTe and CdSe quantum dots for photothermal cancer therapy. *Biomaterials* **2012**, *33*, 7071–7083.

[9] Cole, J. R.; Mirin, N. A.; Knight, M. W.; Goodrich, G. P.; Halas, N. J. Photothermal efficiencies of nanoshells and nanorods for clinical therapeutic applications. *J. Phys. Chem. C* **2009**, *113*, 12090–12094.

[10] Dickerson, E. B.; Dreaden, E. C.; Huang, X. H.; El-Sayed, I. H.; Chu, H. H.; Pushpanketh, S.; McDonald, J. F.; El-Sayed, M. A. Gold nanorod assisted near-infrared plasmonic photothermal therapy (PPTT) of squamous cell carcinoma in mice. *Cancer Lett.* **2008**, *269*, 57–66.

[11] Fisher, J. W.; Sarkar, S.; Buchanan, C. F.; Szot, C. S.; Whitney, J.; Hatcher, H. C.; Torti, S. V.; Rylander, C. G.; Rylander, M. N. Photothermal response of human and murine cancer cells to multiwalled carbon nanotubes after laser irradiation. *Cancer Res.* **2010**, *70*, 9855–9864.

[12] Hessel, C. M.; Pattani, V. P.; Rasch, M.; Panthani, M. G.; Koo, B.; Tunnell, J. W.; Korgel, B. A. Copper selenide nanocrystals for photothermal therapy. *Nano Lett.* **2011**, *11*, 2560–2566.

[13] Huang, X. Q.; Tang, S. H.; Liu, B. J.; Ren, B.; Zheng, N. F. Enhancing the photothermal stability of plasmonic metal nanoplates by a core–shell architecture. *Adv. Mater.* **2011**, *23*, 3420–3425.

[14] Yang, J.; Choi, J.; Bang, D.; Kim, E.; Lim, E.-K.; Park, H.; Suh, J.-S.; Lee, K.; Yoo, K.-H.; Kim, E.-K.; et al. Convertible organic nanoparticles for near-infrared photothermal ablation of cancer cells. *Angew. Chem. Int. Ed.* **2011**, *50*, 441–444.

[15] Jain, P. K.; Huang, X. H.; El-Sayed, I. H.; El-Sayed, M. A. Noble metals on the nanoscale: Optical and photothermal properties and some applications in imaging, sensing, biology, and medicine. *Acc. Chem. Res.* **2008**, *41*, 1578–1586.

[16] Lambert, T. N.; Andrews, N. L.; Gerung, H.; Boyle, T. J.; Oliver, J. M.; Wilson, B. S.; Han, S. M. Water-soluble germanium(0) nanocrystals: Cell recognition and near-infrared photothermal conversion properties. *Small* **2007**, *3*, 691–699.

[17] Tang, S. H.; Huang, X. Q.; Zheng, N. F. Silica coating improves the efficacy of Pd nanosheets for photothermal therapy of cancer cells using near infrared laser. *Chem. Commun.* **2011**, *47*, 3948–3950.

[18] Tian, Q. W.; Jiang, F. R.; Zou, R. J.; Liu, Q.; Chen, Z. G.; Zhu, M. F.; Yang, S. P.; Wang, J. L.; Wang, J. H.; Hu, J. Q. Hydrophilic Cu_9S_5 nanocrystals: A photothermal agent with a 25.7% heat conversion efficiency for photothermal ablation of cancer cells *in vivo*. *ACS Nano* **2011**, *5*, 9761–9771.

[19] Tian, Q. W.; Tang, M. H.; Sun, Y. G.; Zou, R. J.; Chen, Z. G.; Zhu, M. F.; Yang, S. P.; Wang, J. L.; Wang, J. H.; Hu, J. Q. Hydrophilic flower-like CuS superstructures as an efficient 980 nm laser-driven photothermal agent for ablation of cancer cells. *Adv. Mater.* **2011**, *23*, 3542–3547.

[20] Yang, K.; Zhang, S.; Zhang, G. X.; Sun, X. M.; Lee, S.-T.; Liu, Z. Graphene in mice: Ultrahigh *in vivo* tumor uptake and efficient photothermal therapy. *Nano. Lett.* **2010**, *10*, 3318–3323.

[21] Lim, D.-K.; Barhoumi, A.; Wylie, R. G.; Reznor, G.; Langer, R. S.; Kohane, D. S. Enhanced photothermal effect of plasmonic nanoparticles coated with reduced graphene oxide. *Nano Lett.* **2013**, *13*, 4075–4079.

[22] Li, J.; Jiang, F.; Yang, B.; Song, X.-R.; Liu, Y.; Yang, H.-H.; Cao, D.-R.; Shi, W.-R.; Chen, G.-N. Topological insulator bismuth selenide as a theranostic platform for simultaneous cancer imaging and therapy. *Sci. Rep.* **2013**, *3*, 1998.

[23] Ai, K. L.; Liu, Y. L.; Liu, J. H.; Yuan, Q. H.; He, Y. Y.; Lu, L. H. Large-scale synthesis of Bi_2S_3 nanodots as a contrast agent for *in vivo* X-ray computed tomography imaging. *Adv. Mater.* **2011**, *23*, 4886–4891.

[24] Kinsella, J. M.; Jimenez, R. E.; Karmali, P. P.; Rush, A. M.; Kotamraju, V. R.; Gianneschi, N. C.; Ruoslahti, E.; Stupack,

D.; Sailor, M. J. X-ray computed tomography imaging of breast cancer by using targeted peptide-labeled bismuth sulfide nanoparticles. *Angew. Chem. Int. Ed.* **2011**, *50*, 12308–12311.

[25] Rabin, O.; Perez, J. M.; Grimm, J.; Wojtkiewicz, G.; Weissleder, R. An X-ray computed tomography imaging agent based on long-circulating bismuth sulphide nanoparticles. *Nat. Mater.* **2006**, *5*, 118–122.

[26] Chang, K.; Lou, W.-K. Helical quantum states in HgTe quantum dots with inverted band structures. *Phys. Rev. Lett.* **2011**, *106*, 206802.

[27] Kim, N.; Lee, P.; Kim, Y.; Kim, J. S.; Kim, Y.; Noh, D. Y.; Yu, S. U.; Chung, J.; Kim, K. S. Persistent topological surface state at the interface of Bi_2Se_3 film grown on patterned graphene. *ACS Nano* **2014**, *8*, 1154–1160.

[28] Liu, H. W.; Jiang, H.; Sun, Q.-F.; Xie, X. C. Dephasing effect on backscattering of helical surface states in 3D topological insulators. *Phys. Rev. Lett.* **2014**, *113*, 046805.

[29] Moore, J. E. The birth of topological insulators. *Nature* **2010**, *464*, 194–198.

[30] Reijnders, A. A.; Tian, Y.; Sandilands, L. J.; Pohl, G.; Kivlichan, I. D.; Zhao, S. Y. F.; Jia, S.; Charles, M. E.; Cava, R. J.; Alidoust, N.; et al. Optical evidence of surface state suppression in Bi-based topological insulators. *Phys. Rev. B* **2014**, *89*, 075138.

[31] Wang, L.-L.; Huang, M. L.; Thimmaiah, S.; Alam, A.; Bud'ko, S. L.; Kaminski, A.; Lograsso, T. A.; Canfield, P.; Johnson, D. D. Native defects in tetradymite $Bi_2(Te_xSe_{3-x})$ topological insulators. *Phys. Rev. B* **2013**, *87*, 125303.

[32] Ghaemi, P.; Mong, R. S. K.; Moore, J. E. In-plane transport and enhanced thermoelectric performance in thin films of the topological insulators Bi_2Te_3 and Bi_2Se_3. *Phys. Rev. Lett.* **2010**, *105*, 166603.

[33] Ghosh, S.; Dutta, S.; Gomes, E.; Carroll, D.; D'Agostino, R.; Olson, J.; Guthold, M.; Gmeiner, W. H. Increased heating efficiency and selective thermal ablation of malignant tissue with DNA-encased multiwalled carbon nanotubes. *ACS Nano* **2009**, *3*, 2667–2673.

[34] Chen, J. Y.; Yang, M. X.; Zhang, Q.; Cho, E. C.; Cobley, C. M.; Kim, C.; Glaus, C.; Wang, L. H. V.; Welch, M. J.; Xia, Y. N. Gold nanocages: A novel class of multifunctional nanomaterials for theranostic applications. *Adv. Funct. Mater.* **2010**, *20*, 3684–3694.

[35] Chen, H. J.; Shao, L.; Ming, T.; Sun, Z. H.; Zhao, C. M.; Yang, B. C.; Wang, J. F. Understanding the photothermal conversion efficiency of gold nanocrystals. *Small* **2010**, *6*, 2272–2280.

[36] Kim, D.; Jeong, Y. Y.; Jon, S. A drug-loaded aptamer-gold nanoparticle bioconjugate for combined CT imaging and therapy of prostate cancer. *ACS Nano* **2010**, *4*, 3689–3696.

[37] Roper, D. K.; Ahn, W.; Hoepfner, M. Microscale heat transfer transduced by surface plasmon resonant gold nanoparticles. *J. Phys. Chem. C* **2007**, *111*, 3636–3641.

[38] Alkilany, A. M.; Nagaria, P. K.; Hexel, C. R.; Shaw, T. J.; Murphy, C. J.; Wyatt, M. D. Cellular uptake and cytotoxicity of gold nanorods: Molecular origin of cytotoxicity and surface effects. *Small* **2009**, *5*, 701–708.

[39] Loo, C.; Lin, A.; Hirsch, L.; Lee, M.-H.; Barton, J.; Halas, N. J.; West, J.; Drezek, R. Nanoshell-enabled photonics-based imaging and therapy of cancer. *Technol. Cancer Res. Treat.* **2004**, *3*, 33–40.

[40] Li, H.; Cao, J.; Zheng, W. S.; Chen, Y. L.; Wu, D.; Dang, W. H.; Wang, K.; Peng, H. L.; Liu, Z. F. Controlled synthesis of topological insulator nanoplate arrays on mica. *J. Am. Chem. Soc.* **2012**, *134*, 6132–6135.

[41] Chen, C.-C.; Herhold, A. B.; Johnson, C. S.; Alivisatos, A. P. Size dependence of structural metastability in semiconductor nanocrystals. *Science* **1997**, *276*, 398–401.

[42] Son, D. H.; Hughes, S. M.; Yin, Y. D.; Alivisatos, A. P. Cation exchange reactions in ionic nanocrystals. *Science* **2004**, *306*, 1009–1012.

[43] Ivanov, S. A.; Piryatinski, A.; Nanda, J.; Tretiak, S.; Zavadil, K. R.; Wallace, W. O.; Werder, D.; Klimov, V. I. Type-II core/shell CdS/ZnSe nanocrystals: Synthesis, electronic structures, and spectroscopic properties. *J. Am. Chem. Soc.* **2007**, *129*, 11708–11719.

[44] Chen, C.-Y.; Cheng, C.-T.; Lai, C.-W.; Hu, Y.-H.; Chou, P.-T.; Chou, Y.-H.; Chiu, H.-T. Type-II CdSe/CdTe/ZnTe (core–shell–shell) quantum dots with cascade band edges: The separation of electron (at CdSe) and hole (at ZnTe) by the CdTe layer. *Small* **2005**, *1*, 1215–1220.

[45] Allione, M.; Ballester, A.; Li, H. B.; Comin, A.; Movilla, J. L.; Climente, J. I.; Manna, L.; Moreels, I. Two-photon-induced blue shift of core and shell optical transitions in colloidal CdSe/CdS quasi-type II quantum rods. *ACS Nano* **2013**, *7*, 2443–2452.

[46] Zhu, H. M.; Song, N. H.; Lian, T. Q. Wave function engineering for ultrafast charge separation and slow charge recombination in type-II core/shell quantum dots. *J. Am. Chem. Soc.* **2011**, *133*, 8762–8771.

[47] Balet, L. P.; Ivanov, S. A.; Piryatinski, A.; Achermann, M.; Klimov, V. I. Inverted core/shell nanocrystals continuously tunable between type-I and type-II localization regimes. *Nano Lett.* **2004**, *4*, 1485–1488.

[48] Zhang, Y.; He, K.; Chang, C.-Z.; Song, C.-L.; Wang, L.-L.; Chen, X.; Jia, J.-F.; Fang, Z.; Dai, X.; Shan, W.-Y.; et al.

Crossover of the three-dimensional topological insulator Bi_2Se_3 to the two-dimensional limit. *Nat. Phys.* **2010**, *6*, 584–588.

[49] Vargas, A.; Basak, S.; Liu, F. Z.; Wang, B. K.; Panaitescu, E.; Lin, H.; Markiewicz, R.; Bansil, A.; Kar, S. The changing colors of a quantum-confined topological insulator. *ACS Nano* **2014**, *8*, 1222–1230.

[50] Smith, A. M.; Mohs, A. M.; Nie, S. M. Tuning the optical and electronic properties of colloidal nanocrystals by lattice strain. *Nat. Nanotechnol.* **2009**, *4*, 56–63.

[51] Kim, S.; Fisher, B.; Eisler, H. J.; Bawendi, M. Type-II quantum dots: CdTe/CdSe(core/shell) and CdSe/ZnTe(core/shell) heterostructures. *J. Am. Chem. Soc.* **2003**, *125*, 11466–11467.

[52] Bang, J.; Park, J.; Lee, J. H.; Won, N.; Nam, J.; Lim, J.; Chang, B. Y.; Lee, H. J.; Chon, B.; Shin, J.; et al. ZnTe/ZnSe (core/shell) type-II quantum dots: Their optical and photovoltaic properties. *Chem. Mater.* **2010**, *22*, 233–240.

[53] Chang, K.; Xia, J.-B. Spatially separated excitons in quantum-dot quantum well structures. *Phys. Rev. B* **1998**, *57*, 9780–9786.

[54] Nemchinov, A.; Kirsanova, M.; Hewa-Kasakarage, N. N.; Zamkov, M. Synthesis and characterization of type-II ZnSe/CdS core/shell nanocrystals. *J. Phys. Chem. C* **2008**, *112*, 9301–9307.

[55] Oron, D.; Kazes, M.; Banin, U. Multiexcitons in type-II colloidal semiconductor quantum dots. *Phys. Rev. B* **2007**, *75*, 035330.